

Chapter 3: Numerical simulation of deformability cytometry - transport of a biological cell through a microfluidic channel

Lucas Daniel Wittwer^{a,b}, Felix Reichel^b, Sebastian Aland^{a,c}

^a*HTW Dresden, Friedrich-List-Platz 1, 01069 Dresden, Germany*

^b*MPL & MPZPM Erlangen, Staudtstrasse 2, 91058 Erlangen, Germany*

^c*TU Bergakademie Freiberg, Akademiestrasse 6, 09599 Freiberg, Germany*

Contents

3.1 Introduction	3
3.2 Modelling Biological Cells in an RT-DC Channel	6
3.3 Hydrodynamic Stresses on the Cell Surface	11
3.4 Cell Shapes and Cell Deformation	15
3.5 Extraction of the Cell Viscosity	22
3.6 Approximation Error of the Cell Volume over the Channel	25
3.7 Conclusions	27
Appendix 3A Derivation of the Deformation Measure from Cell Contours	28

Abstract

Deformability cytometry is an important technique for label-free morphology-based characterisation of large biological cell populations by physical properties. Numerical simulations are needed to extract mechanical properties of the measured cells which deform due to the hydrodynamic stress. Here, we look at Real-Time Deformability-Cytometry (RT-DC) and extend the existing numerical models to take into account the correct three-dimensional geometry of the microfluidic chip as well as the time-dependent viscoelastic behaviour. To this extent, the correct inflow and outflow of the narrow channel are considered and we solve the full bi-directional interaction between the non-Newtonian fluid of the extra-cellular medium and the viscoelastic cell. The findings are compared to the results of previous works that assume axisymmetric flow and the limits of this approximation are discussed. We then analyse the stresses acting on the cell surface as well as the resulting deformations of the cell and explore the effect of higher cell viscosities on the deformation at the outflow. Finally, we propose an improved methodology to extract cytoplasmic viscosity based on experimentally observable shape relaxation inside the channel. Our results explain discrepancies in current viscosity extraction from experimental measurements. With this most complete numerical description of RT-DC, to date, we pave the way for the full viscoelastic characterisation of biological cells in high throughput experiments.

Keywords: microfluidics, RT-DC, Kelvin-Voigt material, fluid-solid-interaction, finite-element method

3.1. Introduction

Cell mechanical properties are important label-free biomarkers that characterise and phenotype cell populations. For example, cell stiffness and deformability are intrinsic quantities determined predominantly by the cytoskeleton and alterations thereof (Pegoraro et al., 2017; Fletcher and Mullins, 2010). Based on internal changes in cell organisation, the cellular state (e.g. cell-cycle (Otto et al., 2015; Chan et al., 2015) or differentiation (Urbanska et al., 2017; Darling et al., 2008; Ekpenyong et al., 2012)), function (e.g. immunoreaction (Vicente-Manzanares and Sánchez-Madrid, 2004)) and dysfunction (e.g. cancer malignancy (Guck et al., 2005)) can be identified without labelling bio-markers by e.g. fluorescence dyes.

Traditional single-cell methods to probe cell mechanical properties include micropipette aspiration (Hochmuth, 2000), atomic force microscopy (AFM) (Binnig et al., 1986; Radmacher, 2007) and optical stretching (Guck et al., 2000, 2001); the measurement rates of these methods are limited to a few hundred cells per hour only (Wu et al., 2018). Recent developments in microfluidic-based high-throughput deformability cytometry enable measurements of large numbers of suspended cells in order to analyse whole cell populations (Urbanska et al., 2020). Real-Time Deformability-Cytometry (*RT-DC*), is such a microfluidic-based technique that is capable of measurement rates up to thousand cells per second (Otto et al., 2015). This technique allows researchers to characterise homogeneous cell populations and also to detect rare cell types that can occur in a medium comprising a heterogeneous cell population, for example blood (Toepfner et al., 2018). In *RT-DC* cells are flushed through a narrow channel within a microfluidic chip and they deform due to the hydrodynamic stresses. A high-speed camera takes images of the cells at the end of a narrow channel where the cells reach a stationary deformation. Morphological features (e.g. size or deformability) are determined from these images and the apparent Young's modulus (Mietke et al., 2015; Mokbel et al., 2017) and other statistics can be obtained (Herbig et al., 2018). Several extensions to *RT-DC* include the addition of fluorescence for biochemical marker identification (*RT-FDC*) (Rosendahl et al., 2018), deep-learning based feature extraction (Kräter et al., 2021) and active sorting capabilities (Nawaz et al., 2020). These make *RT-DC* an even more versatile tool for cell mechanics research and medical diagnostics. Recently, Fregin

et al. (2019) introduced *dynamic RT-DC (dRT-DC)* which extends RT-DC to determine not only cell stiffness, but also the apparent viscoelastic behaviour of the cell by taking several images through the channel.

Eukaryotic cells are composed of a multitude of components that contribute to the mechanical properties of the cell. For example, the cell cortex is a thin active pre-stressed polymer network mainly consisting of actin and myosin (Fischer-Friedrich et al., 2016). The molecular configuration of this polymer network can adapt to internal and external stresses, resulting in a frequency-dependent stress-strain response. On the other hand, the cytosol within the cell is a fluid like material surrounding the nucleus and different organelles which in turn have varying mechanical properties. Depending on the considered time- and length-scale and applied forces, cells have been observed to behave in a manner that could be characterized as elastic, viscoelastic, viscous, or even plastic (Pegoraro et al., 2017; Nawaz et al., 2012; Mokbel et al., 2020; Fischer-Friedrich et al., 2016; Dupire et al., 2020; Bonakdar et al., 2016; Taubenberger et al., 2020). Therefore, the reported values of the cell mechanical properties, like apparent elasticity and viscosity, vary in several orders of magnitude based on the measurement techniques used (Wu et al., 2018).

Numerical simulations are an important tool to understand the complex, time-dependent response of cells under different loading conditions and to validate theoretical models of cell mechanics. Depending on the time- and length- scales taken into account, different mathematical and numerical models for single-cell behaviour have been proposed (Lim et al., 2006; Rajagopal et al., 2018). Here, we focus on continuum models. A linear elastic bulk material model has been used to simulate AFM measurements (Rheinlaender et al., 2020) or the stationary deformation in an RT-DC channel (Mokbel et al., 2017). For large strain bulk simulations, geometrical non-linearities in the underlying mathematical description need to be taken into account. Hyperelastic material models, like the neo-Hookean or Mooney-Rivlin material, have been applied to AFM measurement simulations and to cells-in-flow setups (Müller et al., 2021; Schuster and Marti, 2021). The effect of the cell cortex on the stationary deformation in an RT-DC channel has been investigated in Mokbel et al. (2017). These authors used a linear elastic shell model with surface tension to represent the cortex and a Newtonian fluid for the cytosol. The influence of the cell nucleus, the cell cytoskeleton and the cell cortex under creeping flow has been investigated in Serrano-Alcalde

et al. (2017) with a model that uses a hyperelastic neo-Hookean bulk composite with a linear elastic shell. However, none of these models include time-dependent behaviour.

In this chapter, a fully three dimensional transient model of the dynamics of a cell passing through an RT-DC channel is developed. We extend the numerical model of Fregin et al. (2019) to take into account the deformed cell geometry and the fully coupled bi-directional loading on the cell surface. Instead of a linear elastic material like in Mokbel et al. (2017), we model the cell as an incompressible neo-Hookean Kelvin-Voigt material because the cells undergo large strains at the inflow and outflow of the narrow channel. We analyse the time-dependent response similar to the work from Schuster and Marti (2021) which used an axisymmetric approximation of the channel geometry. Taking into account the correct square channel geometry of the experimental setup, the model developed in this chapter is the first to predict the transient mechanical behaviour of cells in realistic RT-DC experiments. We use the model to successively analyse the fluid flow, the stress distribution on the cell surface and the evolution of cell deformation. We provide a connection to experimentally measurable parameters and illustrate a pathway to extract viscoelastic cell parameters from time-dependent RT-DC measurements.

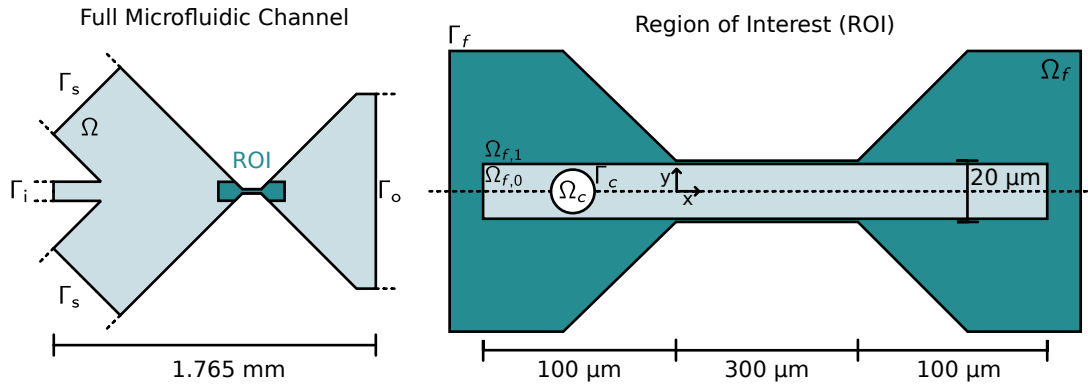


Figure 3.1: **2D Schematic of the Simulation Domain:** (left) Full microfluidic chip Ω with the sample inlet Γ_i and the two sheath flow inlets Γ_s and the outlet Γ_o . The region of interest (ROI) is indicated in darker shade. (right) Magnification of the ROI. The flow profile computed in Ω is set as Dirichlet boundary condition on Γ_f . Ω_f is split into two fluid sub-domains $\Omega_{f,0}$ and $\Omega_{f,1}$, each discretised separately. The cell Ω_c is separated by the interface Γ_c from the surrounding fluid. The origin of the coordinate system is at the inlet into the narrow channel as indicated. The z-axis is normal to the shown schematic. The horizontal dashed line indicates the first symmetry axis.

3.2. Modelling Biological Cells in an RT-DC Channel

The geometric scale of the RT-DC chip with the sample and sheath flow inlet and outlet is on the order of millimetres (see Fig. 3.1). On the other hand, the narrow region where the actual measurements are performed is characterised by length scales that are 1-2 orders of magnitude smaller (tens to hundreds of μm). The cells have a diameter of only a few micrometers and the passage time is a few milliseconds, rendering the problem at hand multi-scale in time and space. Here, we are interested in the cell behaviour between the inflow into the narrow channel and the outflow. In the discussion that follows, the corresponding section of the RT-DC channel is referred to as the *region of interest* or ROI for short (see Fig. 3.1).

In the method presented here, the computational analysis is split into the following three steps. First the correct fluid profile is evaluated in the full microfluidic chip Ω in the absence of cells. In the second step, the method evaluates the coupled fluid-solid interaction between the fluid and the cells at the inlet and within the narrow channel of the ROI. In this step, the flow profile of the previous step is used as boundary condition at the outer boundary Γ_f of the domain Ω_f . In the third step, we model the cell behaviour at the outlet of the ROI separately as explained later.

The three dimensional computational domain of the ROI is split into the fluid domain Ω_f and the subdomain representing the cell Ω_c . The interface between the fluid and solid is denoted

by Γ_c . In the spatial discretisation, the fluid domain Ω_f is split into two separate components: (i) a straight rectangular domain $\Omega_{f,0}$ enclosing the cell and (ii) the remaining fluid region $\Omega_{f,1}$, with $\Omega_f = \Omega_{f,0} \cup \Omega_{f,1}$. Only the mesh of $\Omega_{f,0}$ will change according to the cell movement and deformation.

3.2.1. The Measurement Buffer as a non-Newtonian Fluid

Measurement buffers used in RT-DC and similar high-throughput microfluidics devices exhibit non-Newtonian rheology (Herold, 2017). Therefore, we model the fluid in Ω and Ω_f by the incompressible Navier-Stokes equations with a shear rate dependent viscosity,

$$\rho_f \frac{\partial \mathbf{u}}{\partial t} + \rho_f (\mathbf{u} \cdot \nabla) \mathbf{u} = \nabla \cdot \sigma_f \quad \text{in } \Omega_f, \quad (3.1)$$

$$\sigma_f = \left(-p \mathbf{I} + \eta_f(\mathbf{u})(\nabla \mathbf{u} + (\nabla \mathbf{u})^T) \right) \quad \text{in } \Omega_f, \quad (3.2)$$

$$\nabla \cdot \mathbf{u} = 0 \quad \text{in } \Omega_f, \quad (3.3)$$

where $\rho_f \in \mathbb{R}$ is the fluid density, \mathbf{u} the fluid velocity, p the pressure, $\mathbf{I} \in \mathbb{R}^{3 \times 3}$ the identity matrix and $\eta_f(\mathbf{u})$ the shear rate dependent viscosity. It is typically assumed that inertial forces have a negligible influence for hydrodynamics at such small length scales due to the small Reynolds number (Mietke et al. (2015)) and it has been shown that under conditions associated with RT-DC flows, the inertial terms have only a mild influence on cell deformation (Mokbel et al., 2017). However, because we include shear-thinning, it is possible that the Reynolds number can locally increase significantly. Thus, to keep the results highly accurate, we include the inertial terms and solve the full Equations (3.1) to (3.3).

The fluid shear-rate dependent behaviour can be described by a power-law non-Newtonian fluid (Herold, 2017). This amounts to the velocity-dependent viscosity

$$\eta_f(\mathbf{u}) = m (\dot{\gamma}(\mathbf{u}))^{n-1} \quad \text{in } \Omega_f, \quad (3.4)$$

where $m \in \mathbb{R}$ is the fluid consistency coefficient, $\dot{\gamma}(\mathbf{u}) = \sqrt{\max(2\mathbf{S}(\mathbf{u}) : \mathbf{S}(\mathbf{u}), 0.001)}$ is the bounded shear rate and $n \in \mathbb{R}$ the flow behaviour index. The strain rate tensor is given by $\mathbf{S}(\mathbf{u}) = \frac{1}{2} (\nabla \mathbf{u} + (\nabla \mathbf{u})^T)$.

3.2.2. The Cell as a Viscoelastic Solid Material

We model the cell as a Kelvin-Voigt material where the elastic branch is assumed to be an incompressible hyperelastic neo-Hookean solid:

$$\rho_s \frac{\partial^2 \mathbf{w}}{\partial t^2} = \nabla \cdot (\sigma_c)^T \quad \text{in } \Omega_c, \quad (3.5)$$

$$\sigma_c = \mathbf{F} S_{\text{tot}} \quad \text{in } \Omega_c, \quad (3.6)$$

where \mathbf{w} is the displacement vector, $\mathbf{F} = \frac{\partial \mathbf{x}}{\partial \mathbf{X}} = \nabla \mathbf{w} + \mathbf{I}$ is the deformation gradient and S_{tot} is the total stress. In the case of a Kelvin-Voigt material, the total stress S_{tot} is given by

$$S_{\text{tot}} = S + \tau \dot{S}_{\text{iso}}, \quad (3.7)$$

where $S = \frac{\partial W_s}{\partial \epsilon}$ is the second Piola-Kirchhoff stress, $\tau = \eta_c/E$ the relaxation time of the viscous branch and \dot{S}_{iso} the time derivative of the isochoric part of the stress. The cell's viscosity η_c and the Young's modulus E are material parameters. The Green-Lagrange strain ϵ is given by

$$\epsilon = \frac{1}{2} (\mathbf{F}^T \mathbf{F} - \mathbf{I}). \quad (3.8)$$

The elastic strain energy density W_s of the neo-Hookean hyperelastic material is

$$W_s = \frac{1}{2} \mu (\bar{I}_1 - 3) + \frac{1}{2} \kappa (J_{el} - 1)^2, \quad (3.9)$$

which is the sum of the isochoric strain energy density (using the isochoric invariant \bar{I}_1) and the volumetric strain energy density (using the elastic volumetric deformation J_{el}). In the case of an incompressible material with the Young's modulus E and Poisson ratio $\nu = 0.5$, the material parameters are given by the Lamé parameter $\mu = \frac{E}{2(1+\nu)} \in \mathbb{R}$ and the bulk modulus $\kappa \in \mathbb{R}$.

3.2.3. Boundary Conditions and Fluid-Solid Coupling

The Navier-Stokes Equations (3.1) to (3.3) are solved in the full chip geometry (Fig. 3.1 left) in the absence of a cell first to get the correct inflow profile for the sub-model of the ROI (Fig. 3.1 right). On the channel wall we enforce no-slip conditions on the velocity field by

$$\mathbf{u} = \mathbf{0}. \quad (3.10)$$

On the chip inlets we set the velocity field according to the experimental setup and we fix the pressure at the outlet by:

$$\mathbf{u} = \mathbf{u}_s \quad \text{on } \Gamma_s, \quad (3.11)$$

$$\mathbf{u} = \mathbf{u}_i \quad \text{on } \Gamma_i, \quad (3.12)$$

$$p = 0 \quad \text{on } \Gamma_o, \quad (3.13)$$

where \mathbf{u}_s and \mathbf{u}_i are the inflow velocity profiles at the sheath and sample inlet. The resulting flow profile is then set as boundary condition at the inflow and outflow Γ_f of the sub-model of the ROI. We monotonically increase the inflow velocity in the first few time steps from zero to the correct velocity profile for stability reasons.

On the interface Γ_c , we impose the kinematic condition (continuity of velocities) and dynamic condition (balance of forces) by

$$\mathbf{u} = \partial_t \mathbf{w} \quad \text{on } \Gamma_c, \quad (3.14)$$

$$\mathbf{n} \cdot \sigma_f = \mathbf{n} \cdot \sigma_c \quad \text{on } \Gamma_c, \quad (3.15)$$

where \mathbf{n} is a normal vector to the fluid-solid interface and σ_f and σ_c are the internal stresses of the fluid and the solid, respectively.

3.2.4. Finite-Element Implementation

The resulting system of equations is discretised by the Finite-Element method using COMSOL Multiphysics®. Symmetry along the y-z and x-z planes can be used to reduce the computational domain fourfold as indicated in Fig. 3.1 resulting in the computational domains shown in Fig. 3.2. Normal to the planes of symmetry the fluid is subjected to the Dirichlet boundary condition:

$$\mathbf{u} \cdot \mathbf{n} = \mathbf{0} \quad (3.16)$$

and similar no-displacement condition of the cell in Ω_c by

$$\mathbf{w} \cdot \mathbf{n} = \mathbf{0}, \quad (3.17)$$

where \mathbf{n} is the normal to the plane of symmetry.

The geometry of the sub-model is discretised with two independent but adjacent meshes for $\Omega_{f,0}$ and $\Omega_{f,1}$. The mesh of $\Omega_{f,1}$ stays fixed throughout the whole simulation. Only the mesh discretising $\Omega_{f,0}$, Ω_c and Γ_c changes with the cell movement and deformation. On the interface between $\Omega_{f,0}$ and $\Omega_{f,1}$ we enforce a flow continuity by $\mathbf{u}_0 = \mathbf{u}_1$ (equal flow field) and $p_0 = p_1$ (equal pressure) where the subscript indicates the two subdomains again. Remeshing did not lead to stable simulations in 3D. Thus, we use an arbitrary Lagrangian-Eulerian (ALE) approach to allow cell movement through the whole narrow channel. The grid movement on Γ_c is smoothly extended into the interior of the domain. To keep the mesh quality high while reducing the degrees of freedom, we discretise the sub-domain $\Omega_{f,0}$ with a combination of prisms and pyramid elements (away from the cell) and tetrahedral elements (around and within the cell). On the fluid-solid interface and the channel wall we added boundary layers to resolve the high gradient in the flow field as well as to better approximate the normal stress component acting on the cell surface. Fig. 3.2 shows an exemplary mesh which was coarsened for illustrative purposes.

To increase the numerical stability we choose linear Lagrange shape functions for the velocity and the pressure field with streamline and crosswind diffusion stabilisation. The hyperelastic cell material is solved with linear shape functions. The fully bi-directional coupled geometrical non-linear system is solved monolithically with a Newton-method in time and the direct solver PARDISO in space in COMSOL Multiphysics®.

Previous works on RT-DC simulations approximate the channel geometry as rotationally symmetric around the x-axis to effectively reduce the computational model to two dimensions. In this case, the channel width is scaled such that the pressure drop over the axisymmetric cylindrical channel is the same as it would be in the real square channel geometry (see the concept of the *equivalent channel radius* in Mietke et al. (2015) and Mokbel et al. (2017)). While the assumption of axisymmetric geometry might be a good approximation within the narrow channel, it is doubtful along the inflow and outflow regions of the ROI because these would assume unrealistic funnel shapes. Here, we resolve the full 3D geometry of real RT-DC channels. To quantify the error induced by the assumption of axisymmetry, we perform additional 2D axisymmetric simulations. Therefore, we use the concept of the *equivalent channel radius* and set the inflow to a normal flow profile that results in the same flow rate as for the full three-dimensional simulations.

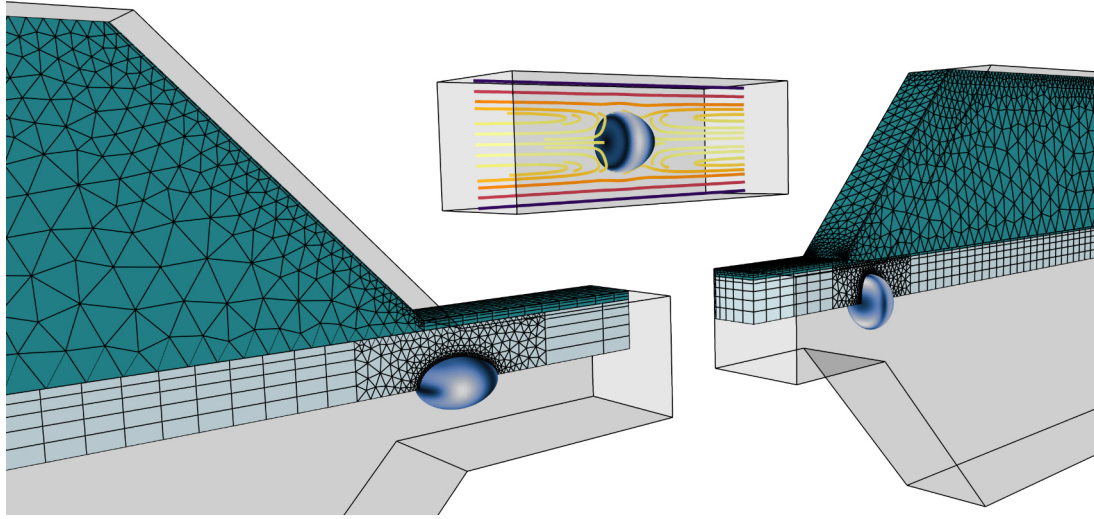


Figure 3.2: **Reduced Computational Domains of the ROI and Streamlines:** Three parts of the ROI are shown: **(left)** Inflow into the narrow channel. The two disjoint domains $\Omega_{f,0}$ and $\Omega_{f,1}$ (see Fig. 3.1) and the barrow containing the cell domain with different element types are shown. The mesh was coarsened for illustrative purposes. The colouring of the cell surface indicates the shear stress. **(middle top)** Stationary deformation at the end of the narrow channel. Streamlines indicate the flow profile relative to the cell motion, coloured by the flow magnitude. **(right)** Outlet from the narrow region.

3.3. Hydrodynamic Stresses on the Cell Surface

In this section we present the first numerical results of a viscoelastic cell traversing a typical RT-DC channel. We successively analyse the fluid flow, corresponding stress distribution on the cell surface, and the resulting evolution of cell deformation.

3.3.1. Fluid Flow in the Microfluidic Chip

To get the correct inflow profile for the sub-model of the ROI, we solve the incompressible Navier-Stokes Equations (3.1) to (3.3) in the full microfluidic chip, taking into account the shear-thinning behaviour of the fluid medium. The fluid is characterised by a density of $\rho_f = 1000 \text{ kg m}^{-3}$, a fluid consistency coefficient of $m = 0.4057 \text{ Pa s}$ and a flow behaviour index of $n = 0.6039$ as described in Equation (3.4). The fluid parameters were measured with an Anton Paar MCR 502 WESP Twindrive rheometer using a 0.3° cone-plate geometry in a shear rate range of $[5000, 50000] \text{ s}^{-1}$.

Fig. 3.3 on the top shows the velocity magnitude and stream lines for a typical RT-DC experimental setup: a sample flow rate of $0.01 \mu\text{l s}^{-1}$ at Γ_i and a sheath flow rate of $0.015 \mu\text{l s}^{-1}$ is prescribed on both parts of Γ_s , resulting in a total flow rate of $0.04 \mu\text{l s}^{-1}$ at the inlets. The pressure

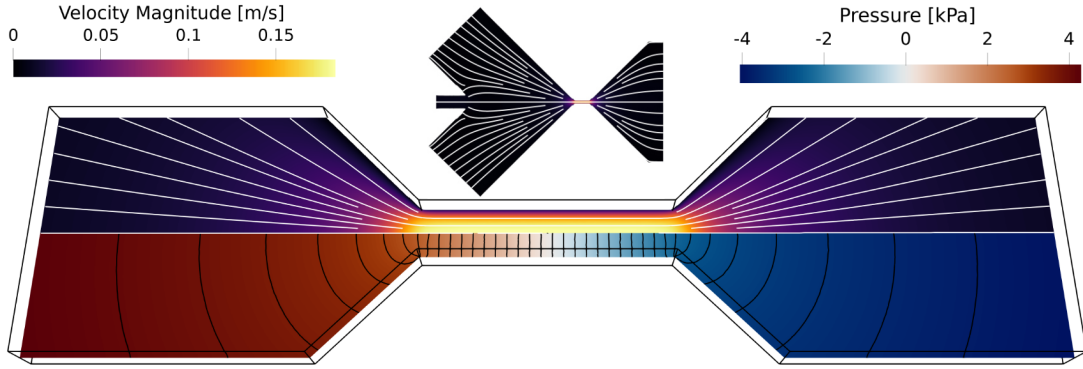


Figure 3.3: **Fluid Flow in the RT-DC Chip: (top centre):** streamlines and the velocity magnitude of the full microfluidic chip. **(bottom)** Horizontal slice through the ROI at $z = 0 \mu\text{m}$. The channel length is shortened to $100 \mu\text{m}$ for demonstration purposes. Upper half: streamlines and velocity magnitude. Lower half: pressure field and isobars along the narrow channel. The pressure is scaled such that it is zero in the centre of the channel at $x = 50 \mu\text{m}$.

is fixed at the centre of the narrow channel to $p = 0 \text{ Pa}$.

The apparent viscosity of the shear-thinning fluid was inferred to be 6 mPa s in a $20 \mu\text{m}$ wide RT-DC chip at a flow rate of $0.04 \mu\text{l s}^{-1}$ based on the derivation of Herold (2017). This is less than half of the 15 mPa s used in (Mietke et al., 2015; Mokbel et al., 2017). The resulting velocity profile at the boundary to the ROI is used as a boundary condition at the inflow and outflow boundaries of the ROI in the forthcoming simulations.

Fig. 3.3 (bottom) shows a close-up of the ROI. The above fluid parameters and flow rate result in a maximum velocity magnitude of 0.184 m s^{-1} in the centre of the channel. This setup is used for all the following simulations.

3.3.2. Deformed Cells in the Region of Interest

Based on the correct inflow profiles computed in the full microfluidic channel, we simulate cellular transport as a bi-directional fluid-solid interaction system in the sub-model of the ROI. The incompressible cells with typical radii of $r \in [3, 5, 7] \mu\text{m}$, a bulk modulus of $\kappa = 2.15 \text{ GPa}$, and density $\rho_c = 1000 \text{ kg m}^{-3}$, start as an undeformed stationary sphere at $x = -80 \mu\text{m}$. Due to the surrounding fluid, cells accelerate, are flushed through the channel and deform based on the complex loading of the hydrodynamic stress. At the same time, the cells alter the fluid flow in their vicinity.

Fig. 3.4 shows the cell shape and the three-dimensional loading on the cell surface as a single cell traverses the ROI. In front of the inlet to the ROI the cell starts as an undeformed sphere. As it

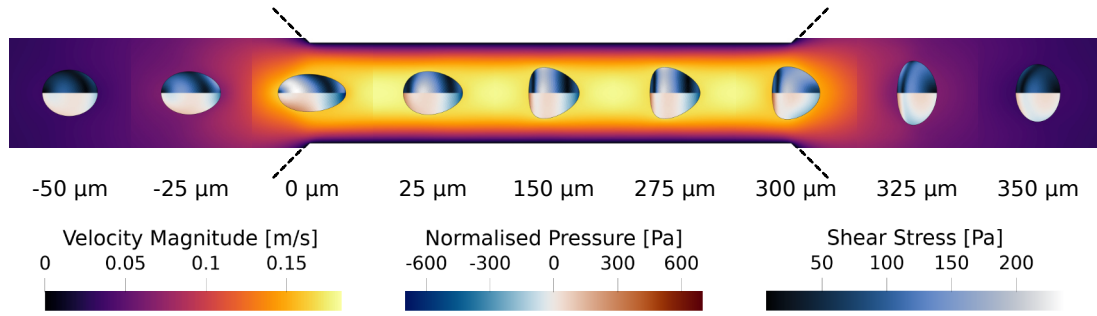


Figure 3.4: **Stresses on the Cell Surface in the ROI:** Cells flowing through the narrow channel (indicated by the dashed lines) from the left to the right. The flow profile is sliced at $z = 0 \mu\text{m}$ and the velocity magnitude is indicated by the colour. The colouring of the cells is split to show the shear stress (top) and the normal pressure stress (bottom) for different cell positions along the channel. The pressure stress is normalised by p_{avg} . Cell parameters: $r = 5 \mu\text{m}$, $E = 1 \text{ kPa}$, $\eta_c = 0.125 \text{ Pa s}$.

approaches the channel inlet, the cell is stretched by the local viscous shear forces so that the cell enters the channel in an elongated form at $x \sim 0 \mu\text{m}$. As the cell proceeds down the channel (and as the flow becomes fully developed), the cell reaches a stationary bullet-shaped configuration where the hydrodynamic and bulk cell forces balance out. The cell shape remains constant through its remaining passage though the narrow channel and the resulting cell shape will be used to derive a deformation measure called *stationary deformation* below. At the outlet of the channel (where the cell is exposed to the outlet flow dynamics), the cell's downstream profile becomes more oblate. After the outlet ($x > 300 \mu\text{m}$) the fluid velocity drops rapidly and the pressure gradient and shear forces decrease, such that the cell returns again to its undeformed spherical shape.

The stresses acting on the cell surface can be decomposed into normal and tangential shear components. In Fig. 3.4 we plot the normal pressure and shear stress on the cell surfaces at different positions in the ROI. The shear stress (indicated in the upper half of the cell) is highest at the inflow ($x = 0 \mu\text{m}$). At the end of the narrow channel, the cell reaches a stationary configuration with a steady cell shape. In this region the shear stress is highest close to the channel wall due to the high shear rate. To visualise the variation, the pressure of each cell in Fig. 3.4 is normalised by subtracting the average surface pressure $p_{\text{avg}} = \frac{\int_{\Gamma_c} p \, dA}{\int_{\Gamma_c} 1 \, dA}$. One can observe that the pressure pushes the cell from the back and pulls it forward at the front. The pressure difference over the cell is largest in the elongated state at the inflow.

The complex loading of the hydrodynamic stress on the cell surface depends on the cell posi-

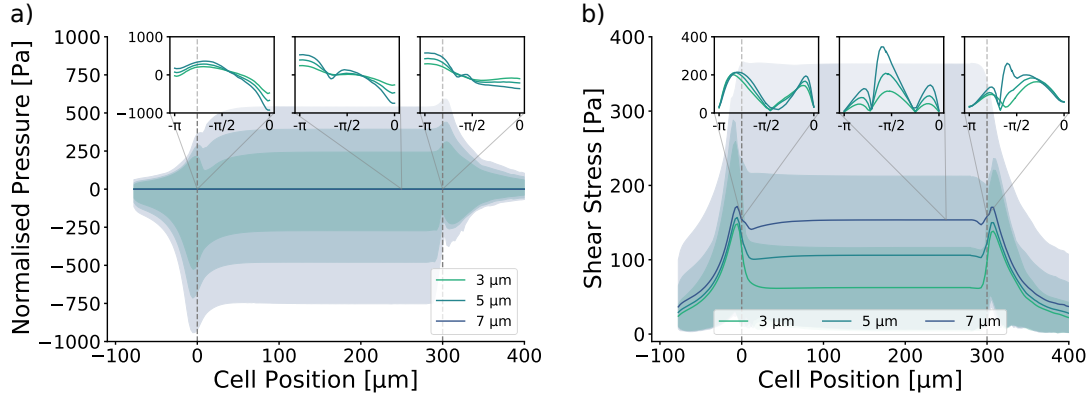


Figure 3.5: **Pressure and Shear Stress on the Cell Contour:** **a)** Average normalised pressure on the cell surface (solid line) with minimal and maximal pressure (filled area) for $r \in [3, 5, 7]\mu\text{m}$. Insets show the normalised pressure distribution on the cell contour over the arc angle θ ($\theta = 0$ is the front of the cell, $\theta = -\pi$ in the back) for three different cell positions $x \in [0, 250, 300]\mu\text{m}$. **b)** Averaged (solid line), minimum and maximum shear stress (filled area) on the cell contour. Insets show the shear stress distribution over the arc angle θ . The channel inlet ($x = 0\mu\text{m}$) and outlet ($x = 300\mu\text{m}$) is indicated by the grey dashed vertical lines. Cell parameters: $E = 1.5 \text{ kPa}$, $\eta_c = 0.125 \text{ Pa s}$.

tion in the ROI. Similar to the stress components shown in Fig. 3.4 on the cell surface, we show the spatial and temporal distribution of pressure and shear stress on the cell contour in Fig. 3.5. We plot the average surface stresses for three different radii $r \in [3, 5, 7]\mu\text{m}$ over the channel position. The shaded area shows the minimum and maximum stresses. One can observe a non-trivial distribution of stresses, with highest absolute values just in front of the inlet and just behind the outlet of the narrow channel. Insets show the stress distributions over the cell contour plotted over the arc angle $\theta \in [0, \pi]$. The pressure is again normalised by the average surface pressure p_{avg} . The surface pressure magnitude increases in the same manner for all three radii and the pressure over the cell is constant as soon as the cell reaches a stationary configuration. The absolute pressure difference across the cell scales with the cell size. After the outlet, the surface pressure drops due to the widening of the channel. On the other hand, the surface shear stress on the cell surface at the inlet does not increase in the same manner for all three radii. The shear stress becomes constant around $x \sim 50 \mu\text{m}$ after channel entry and the shear stress is higher for bigger cells as these come closer to the channel wall.

3.4. Cell Shapes and Cell Deformation

In RT-DC, the cells are imaged with a high-speed camera at a rate of thousands of cells per second. Imaging takes place at the end of the channel where the cells are expected to reach a stationary shape. The camera points in the z -direction, such that each image shows a two-dimensional projection of the cell shape in the xy -plane. These images are used to extract the two-dimensional cell contour from which several shape measures are computed. The cell contour for a cell flowing from the left to the right through the ROI is shown in Fig. 3.6a. The cell starts as an undeformed sphere and gets deformed due to the hydrodynamic stresses on the cell surface as described above.

To extract the apparent Young's modulus, two correlated measures are needed: the area A enclosed by the cell contour and the deformation D . The deformation is defined as

$$D = 1 - \text{circularity} = 1 - \frac{2\sqrt{\pi A}}{L}, \quad (3.18)$$

where L is the circumference of the contour (Otto et al., 2015). An undeformed cell has a deformation value of $D = 0$ and the more the cell shape diverges from a perfect sphere, D increases. The deformation value of the stationary cell shape at the end of the narrow channel (referred to as *stationary deformation*) is independent on the cell viscosity. From each observed area and deformation pair, one can conclude a unique Young's modulus by using a lookup table created by numerical simulations (Mietke et al., 2015; Mokbel et al., 2017).

Here, we are not only interested in the stationary deformation at the end of the channel but also the temporal evolution of the deformation over the full ROI. In Fig. 3.6b we plot the deformation, D , over the ROI for cells with different radii r and Young's moduli E with a fixed viscosity $\eta_c = 0.125$ Pa s. So far, analytical (see Mietke et al. (2015)) as well as numerical models of such microfluidic channels (Mokbel et al., 2017; Schuster and Marti, 2021) assumed an axisymmetric geometry. The axisymmetric assumption might be a good approximation for smaller stationary deformed cells and helps to reduce the computational costs but the stresses acting on larger cells are not rotationally symmetric and the flow profile at the inlet and outlet of the square channel differs from a cylindrical inflow / outflow funnel. Especially the height of the channel does not change and is fixed to $z = 20$ μm . Nevertheless, to compare the behaviour in the cylindrical channel to the square channel we set up the same system as described above in an axisymmetric geometry. As in

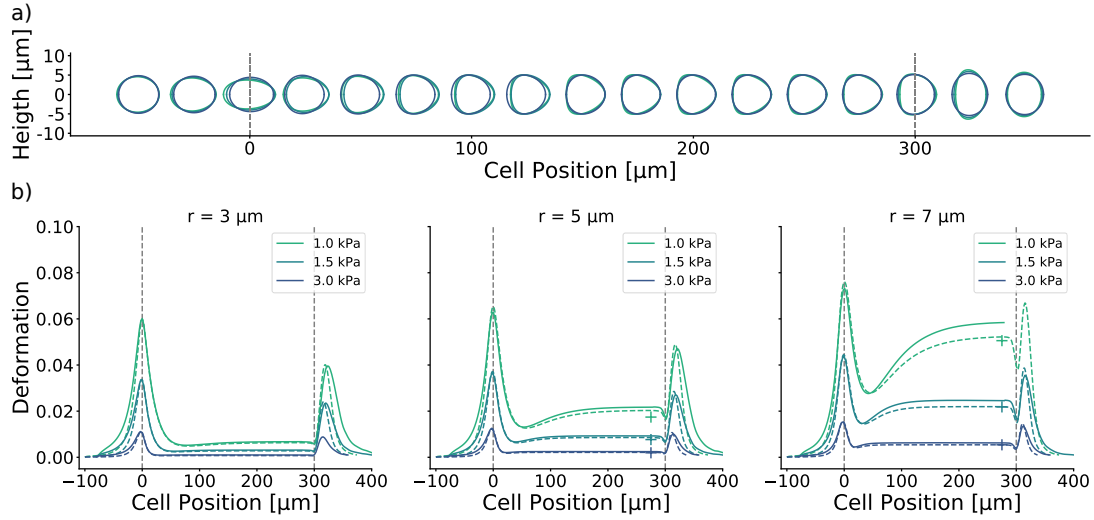


Figure 3.6: **Contours and Deformation Curves for Three Different Young's Moduli:** **a)** Contours for cells with a radius $r = 5 \mu\text{m}$ and three different Young's moduli $E \in [1, 1.5, 3]\text{kPa}$. The cell viscosity is fixed to $\eta_c = 0.125 \text{Pa}\cdot\text{s}$. The channel inlet ($x = 0 \mu\text{m}$) and outlet ($x = 300 \mu\text{m}$) is indicated by the grey dashed vertical lines. See colour legend in b). **b)** Deformation curves for cells with a radius of $3 \mu\text{m}$ (left), $5 \mu\text{m}$ (middle) and $7 \mu\text{m}$ (right). Solid lines show the deformation of the square channel (3D) simulations, dashed lines the cylindrical (axisymmetric) geometry. The stationary deformations of the axisymmetric linear bulk material model at the end of the channel from Mokbel et al. (2017) (derived from (Wittwer et al., 2020)) are indicated with plus signs. This dataset does not contain stationary deformation values for small cells, e.g. with $r = 3 \mu\text{m}$.

previous models (Mietke et al., 2015; Mokbel et al., 2017; Schuster and Marti, 2021) we take into account the *equivalent channel radius*, i.e. the cylindrical channel diameter is chosen by a factor 1.094 larger than the square channel width, to get the same pressure drop along the channel.

The deformations peak at the channel inlet and relax to a stationary deformation in the narrow channel in agreement with the experimental observation in (Fregin et al., 2019). Depending on the cell stiffness, the deformation curve shows a local minimum just after the inlet before reaching the stationary deformation. At the outlet, the cells start to relax but are compressed due to the fluid slowing down (see Fig. 3.4), leading to a second peak of the deformation. Experimental measurements at lower flow rate and higher fluid viscosity did not indicate such a peak at the outlet (Fregin et al., 2019). Apart from the difference in parameters, this discrepancy might be due the fact that experimental cells are not yet in a stationary deformation at the end of the channel, or due to mechanical effects in the considered cell types which are not captured in our numerical model.

Cells in both virtual geometries, axisymmetric and square channel, show similar behaviour

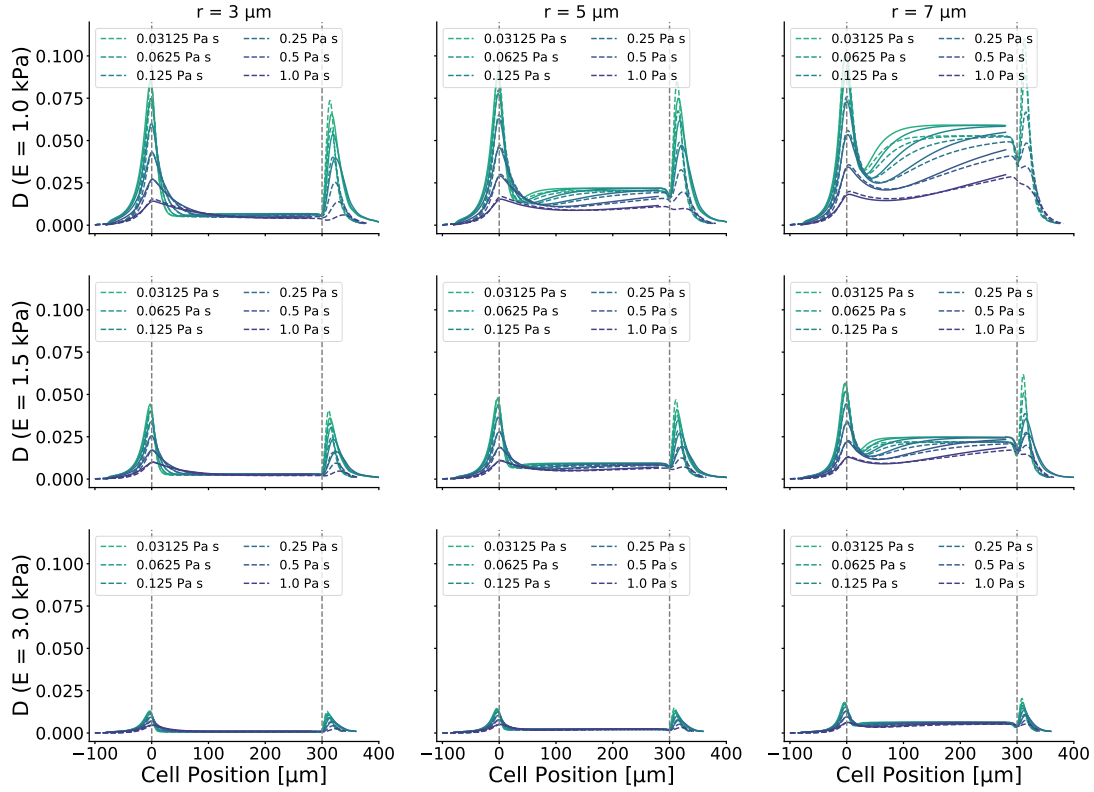


Figure 3.7: **Deformation Curves for Different Cell Radii, Young's Moduli and Viscosities:** From left to the right: The cell radius increases with $r \in [3, 5, 7]\mu\text{m}$. Top to bottom: The cells Young's modulus increases with $E \in [1, 1.5, 3]\text{Pa}$. For each combination of r and E the deformation D for different cell viscosities $\eta_c \in [0.03125, 0.0625, 0.125, 0.25, 0.5, 1]\text{Pa s}$ is shown. Solid lines are the square (3D) channel simulations, dashed lines the axisymmetric cylindrical simulations. The vertical lines indicate the inlet and outlet position.

at the inlet region and in the channel but the relaxation time at the channel outflow differs. The difference between the stationary deformation in the square and the cylindrical channel becomes larger for bigger cell radii, pointing at the limitation of the axisymmetric assumption in the previous works. The peak height and relaxation time to reach the stationary deformation is dependent on the Young's modulus. The relaxation back into a sphere takes longer in the square channel. We cannot simulate the outflow simulation for $r = 7 \mu\text{m}$ and $x = 1 \text{ kPa}$ as the cell touches the boundary of $\Omega_{f,0}$. The linear elastic material model of Mokbel et al. (2017) in the axisymmetric cylindrical channel predicts a lower stationary deformation for softer cells. For stiffer and / or smaller cells the cylindrical model assumption is in good agreement.

The temporal evolution is not only dependent on the cell radius r and Young's modulus E but also on the cell's viscosity η_c . Therefore, we ran a larger parameter sweep not only over

the radius and Young's modulus but also the cell viscosity. We start the simulations with the cells at $x = -100\ \mu\text{m}$ in the cylindrical channel and $x = -80\ \mu\text{m}$ in the square channel. The resulting deformation curves are shown in Fig. 3.7 where we set the bulk viscosity to $\eta_c \in [0.03125, 0.0625, 0.125, 0.25, 0.5, 1]\text{Pa}\cdot\text{s}$ which lies in the typically assumed parameter range of cytosol. For all simulated viscosities the deformation shows a peak at the inflow and outflow. The height of this peak largely depends on the cell viscosity. After the channel inflow, the deformation reaches a local minimum before reaching the stationary value for small viscosities. For higher viscosities this minimum is missing and the cells relax monotonically to the stationary deformation. For small Young's moduli, large cells and highly viscous cells, the deformation does not become stationary within the $300\ \mu\text{m}$ channel. For large and soft cells, the stationary deformation in the cylindrical channel is lower than the deformation in the square channel. This is due to the non-symmetric stresses along the flow direction resulting in an unequal deformation of the cell. The cell's deformation decreases slightly before the actual channel outflow but then increases due to the elongation in the y -direction at the outflow. Whereas in the inflow region, the deformation in the cylindrical and square channel is comparable, the results differ at the outflow, showing an increased peak height for the cylindrical channel. Also, the relaxation to an undeformed state is different, which can be mostly explained by the more pronounced velocity drop in the cylindrical funnel. The relaxation times in the narrow channels are similar for both geometries.

In Fig. 3.8 we fix the radius and plot the deformation evolution for different Young's moduli and viscosities. For all viscosities the deformation curves after the outlet start to align even though the relaxation time in a Kelvin-Voigt model should be unequal. This indicates that the influence of viscosity in the simulated range is negligible and cell deformation is quasi-stationary, determined only by the current hydrodynamic stresses, which the cell experiences.

Note, that we simulate the inflow together with the narrow channel and the outflow separately. Hence, we can only simulate cells in the outflow region which reach a stationary deformation in the narrow channel. Additionally, if the cell elongates too much in the y -direction at the outflow such that it touches the boundary of $\Omega_{f,0}$, the simulation does not reproduce the deformation behaviour correctly or even crashes. Those limitations are most prominent for large cells with low viscosities (upper right corner in Fig. 3.7). For large cells, a model as proposed in Mokbel et al. (2018) would

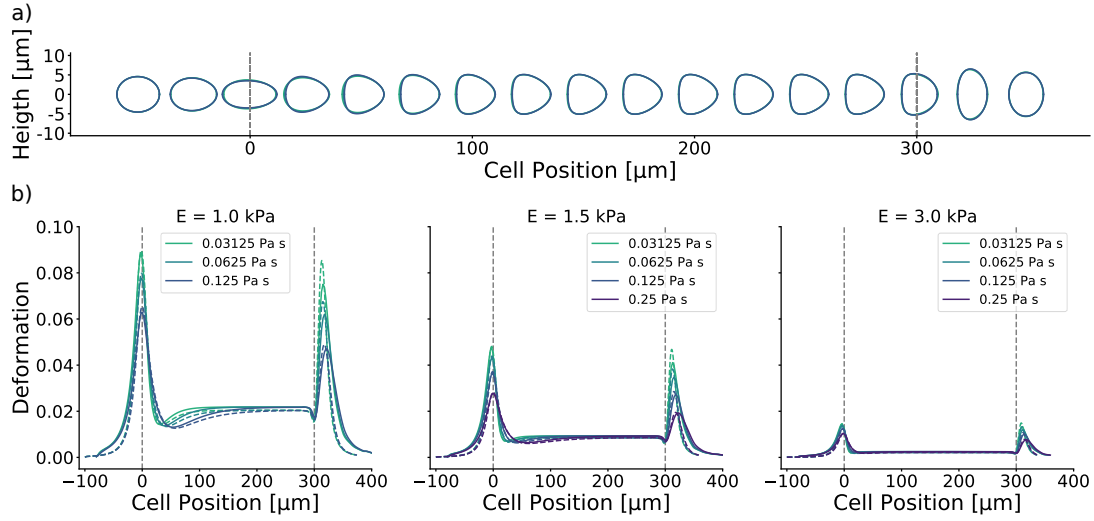


Figure 3.8: **Contours and Deformation Curves for Different Viscosities:** **a)** Contours for cells with a radius $r = 5 \mu\text{m}$ and three different viscosities $\eta_c \in [0.03125, 0.0625, 0.125] \text{Pa s}$. The cell Young's modulus is fixed to $E = 1.0 \text{kPa}$. The channel inlet ($x = 0 \mu\text{m}$) and outlet ($x = 300 \mu\text{m}$) is indicated by the grey dashed vertical lines. See colour legend in b). **b)** Deformation curves for cells with a radius of $5 \mu\text{m}$ and a Young's modulus of 1.0kPa (left), 1.5kPa (middle) and 3.0kPa (right). Solid lines show the deformation of the square channel (3D) simulations, dashed lines the cylindrical (axisymmetric) geometry. The cell with $E = 1.0 \text{kPa}$ and $\eta_c = 0.25 \text{Pa s}$ is not stationary in the narrow channel and thus excluded.

allow for higher deformations at the cost of complexity and increased computational burden.

3.4.1. Deformation of Highly Viscous Cells at the Outflow

The complex stress distribution at the channel inflow renders the task to extract a stress-strain relationship rather complicated. The outflow of the narrow channel on the other hand is more interesting: the cells are pre-stressed into a stationary deformation and relax to the undeformed configuration. Under the assumption that the narrow channel is long enough for even higher viscosities as presented so far, we simulated the channel outflow with cells up to $\eta_c = 4 \text{Pa s}$ fixing the cell radius to $r = 5 \mu\text{m}$ and the Young's modulus to $E = 1 \text{kPa}$. The different deformation curves for the square channel are shown in Fig. 3.9. Cells with small viscosities show a small local minimum followed by a larger local maximum already discussed above. But cells with viscosities of $\eta_c > 1 \text{Pa s}$ do not show this alternation but relax monotonically back into a sphere.

3.4.2. Inertia Ratio and Fourier Transcriptors

Besides the deformation measure defined above, several other ways exist to describe the deformed cell shapes. Here, we summarise two of those measures, the inertia ratio and Fourier transcriptors,

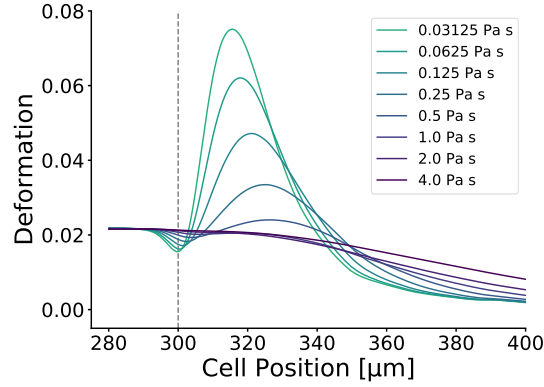


Figure 3.9: **High Viscosity Outflow Behaviour** Deformation values at the outlet (vertical dashed grey line) for cell viscosities $\eta_c \in [0.03125, 0.0625, 0.125, 0.25, 0.5, 1, 2, 4]$ Pa s in the square channel. The Young's modulus is fixed to $E = 1$ kPa and the radius to $r = 5$ μm .

and plot them over the channel.

The cell deformation, D , based on the cells circularity does not capture information about the principal stretches of the deformed cell. This information is described in the ratio of the two eigenvalues of the moment-of-area tensor, called *inertia ratio* (Mokbel et al., 2017). In contrast to the deformation which is evaluated on the detected contour, the inertia ratio is based on two integrals over the cell area. Thus, being a quantity based on integrals, it is more robust against noise in the experimental data. Here we use the definition of the inertia ratio that is available in the standard RT-DC software, dclab (Müller et al., 2015), which for horizontally symmetric shapes is defined by

$$I = \sqrt{\frac{I_{yy}}{I_{xx}}}, \quad (3.19)$$

$$I_{xx} = \int_A (y - y_b)^2 dA, \quad (3.20)$$

$$I_{yy} = \int_A (x - x_b)^2 dA, \quad (3.21)$$

where A is the cell domain and (x_b, y_b) is the cell barycentre (Herbig et al., 2018). The derivation of the inertia ratio based on the cell contour data is described in Appendix 3A.

Fig. 3.10 shows the inertia ratio for different radii and viscosities plotted over the channel position. An inertia ratio of $I > 1$ indicates a cell elongated along the x-axis, an inertia ratio of $I < 1$ an elongation along the y-axis. The inertia ratio is $I \approx 1$ if there is no dominant principal

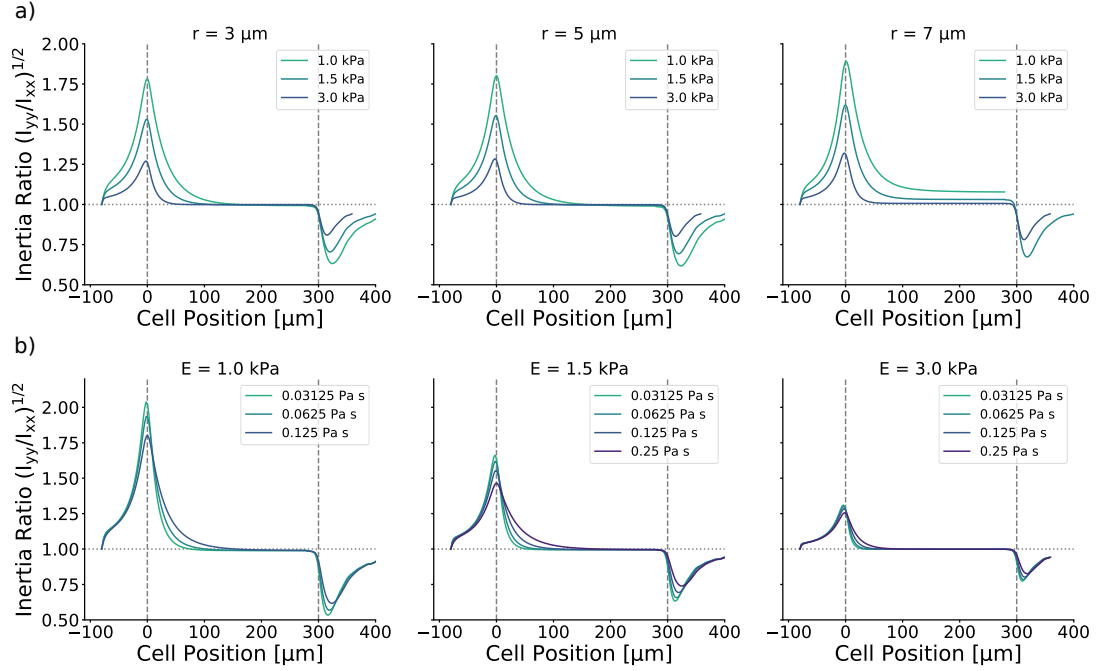


Figure 3.10: **Inertia Ratio for different Young's moduli and cell viscosities:** **a)** Inertia ratio $I = \sqrt{\frac{I_{xx}}{I_{yy}}}$ for three different Young's moduli $E \in [1, 1.5, 3]$ kPa and cell sizes $r \in [3, 5, 7]$ μm . The cell viscosity is fixed to $\eta_c = 0.125$ Pa s. Vertical dashed lines indicate channel inlet and outlet. Horizontal dotted lines indicate an inertia ratio of $I = 1$. **b)** Inertia ratio for different viscosities and Young's moduli. The cell radius is fixed to $r = 5$ μm .

stretch direction. In contrast to the deformation D , the inertia ratio does not show a local minimum after the channel entry, and may therefore be better suited to extract cellular relaxation times and cellular viscosity out of RT-DC measurements, as we will show in Sec. 3.5. At the outflow, the inertia ratio shows a local minimum when the cells elongate in the y -direction. The downside of using the inertia ratio to measure the stationary deformation is that it does not depend uniquely on the Young's modulus (see Mokbel et al. (2017)). Thus, extracting the apparent Young's modulus might not be possible for certain measurements.

To decouple the elongation at the inlet, resulting from the velocity increase in x -direction, from the bullet shape caused by the shear stresses in the channel, Fregin et al. (2019) proposed to decompose the cell contour by the discrete Fourier transform (see Appendix 3A). Reconstructing the contours with only the odd coefficients of the Fourier modes, the new shapes do not exhibit the elongation because the information about the ellipticity of the cell is stored in the even coefficients only. Based on the contours reconstructed from either the even or odd coefficients only, we can

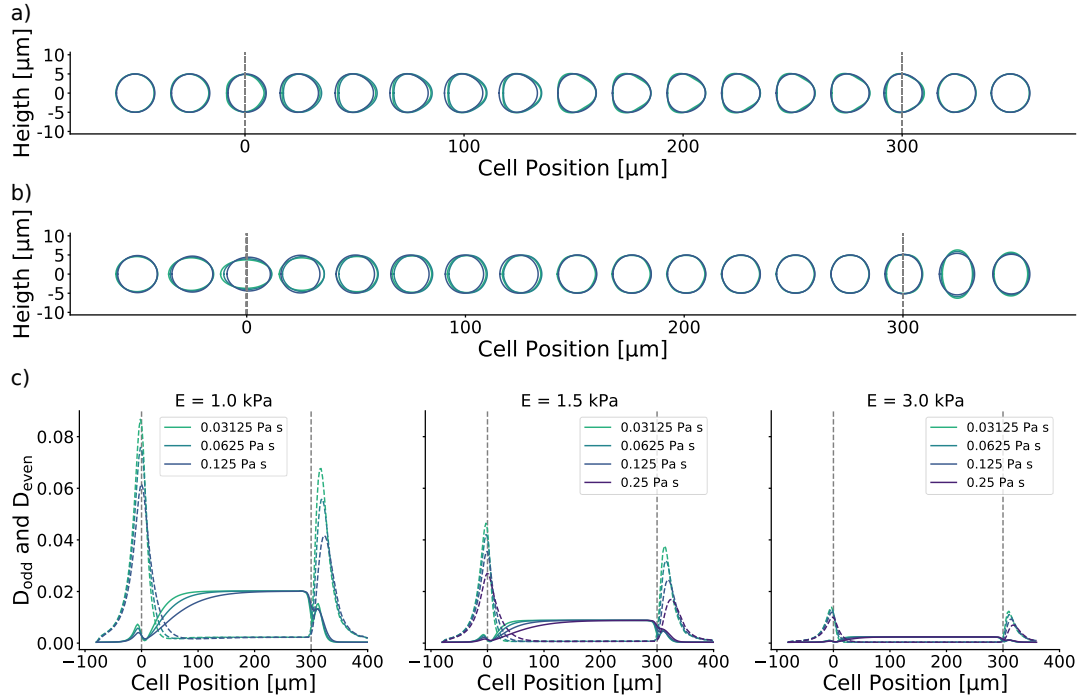


Figure 3.11: **Even and Odd Cell Contours from Fourier Decomposition:** **a)** Cell contours reconstructed from the odd Fourier coefficients for cells with a radius $r = 5 \mu\text{m}$ and three different viscosities $\eta_c \in [0.03125, 0.625, 0.125]\text{Pa s}$. The channel inlet ($x = 0 \mu\text{m}$) and outlet ($x = 300 \mu\text{m}$) is indicated by the grey dashed vertical lines. **b)** Contours reconstructed from the even Fourier coefficients for the same parameters. In both cases the contours are reconstructed with $k \leq 9$ Fourier coefficients. See colour legend in c). **c)** Deformation curves D_{odd} (solid lines) and D_{even} (dashed lines) of the contours reconstructed from the odd and even coefficients only for cells with a radius of $5 \mu\text{m}$ and a Young's modulus of 1.0 kPa (left), 1.5 kPa (middle) and 3.0 kPa (right).

derive the deformation values D_{even} and D_{odd} . The resulting contours over the full microfluidic channel are shown in Fig. 3.11a and Fig. 3.11b, the corresponding deformation curves are depicted in Fig. 3.11c.

3.5. Extraction of the Cell Viscosity

To extract the cell viscosity from RT-DC measurements, Fregin et al. (2019) introduced the idea to decouple the shear stress acting on the cell surface into (i) the high shear stress at the inlet due to the acceleration of the fluid in the direction of the channel and (ii) the lower constant shear stress within the narrow channel (see also Fig. 3.5b)

Simplifying the complex stress evolution to a constant step stress throughout the narrow channel reduces the problem to a simple creeping problem. Further assuming the cell to be a Kelvin-Voigt material and reducing its three-dimensional shape to a simple uniaxial problem, the evolution

of strain $\epsilon(t)$ is

$$\epsilon(t) = \epsilon_1 + \epsilon_2 \exp(-t/\tau),$$

where $\epsilon_1 + \epsilon_2$ is the initial strain (at $t = 0$), ϵ_1 is the final (relaxed) strain (as $t \rightarrow \infty$) and $\tau = \frac{\eta_c}{E}$ is the viscoelastic relaxation time. The idea for extraction of the cell viscosity is to fit the above strain evolution to the experimentally observed evolution of deformation, with the free parameters ϵ_1 , ϵ_2 and τ . The parameter τ which provides the best fit is referred to as the apparent relaxation time τ_a . Together with the apparent Young's modulus E_a this allows to extract the apparent viscosity $\eta_a = E_a \tau_a$. In experimental data, the apparent Young's modulus E_a can be extracted from the stationary deformation within the narrow channel such that the whole methodology can be applied to extract the viscosity from experimental data, as proposed by Fregin et al. (2019). The different deformation measures introduced in the previous section can be used to identify the strain.

Next, we challenge this methodology for the first time by comparing extracted viscosity to the actual simulated viscosity. As strain measures we use the squared inertia ratio, $\epsilon = I^2$ and the even and uneven deformations, $\epsilon = D_{\text{even}}$ and $\epsilon = D_{\text{odd}}$, respectively. We find that the deformation D itself is not suited for this analysis as it does not monotonically relax after the channel inlet (see Fig. 3.8). The fitted curves for the different deformation measures are shown in Fig. 3.12a. We fit the relaxation curve starting at $x = 50 \mu\text{m}$ to exclude the influence from the inlet. Fitting the curve earlier in the channel does not alter the result significantly. The above approach does work for higher viscosities which do not reach stationary deformation at the end of the narrow channel. Thus, here we use the simulated data from the inflow until $x = 300 \mu\text{m}$ which contains simulated viscosities up to 1 Pa s.

In Fig. 3.12b(left) we depict the actual cell viscosity η_c in comparison to the apparent viscosity η_a extracted from the three different strain measures, D_{even} , D_{odd} and I^2 . It can be seen that the viscosity extraction based on the inertia ratio I^2 gives a quite accurate approximation, while the results based on D_{even} and D_{odd} deviate significantly from the actual viscosity. Our results show the limits of viscosity extraction based on D_{even} and D_{odd} and finally explain the experimental finding in Fregin et al. (2019) that viscosity extraction based on D_{even} led to significantly lower apparent viscosity than based on D_{odd} .

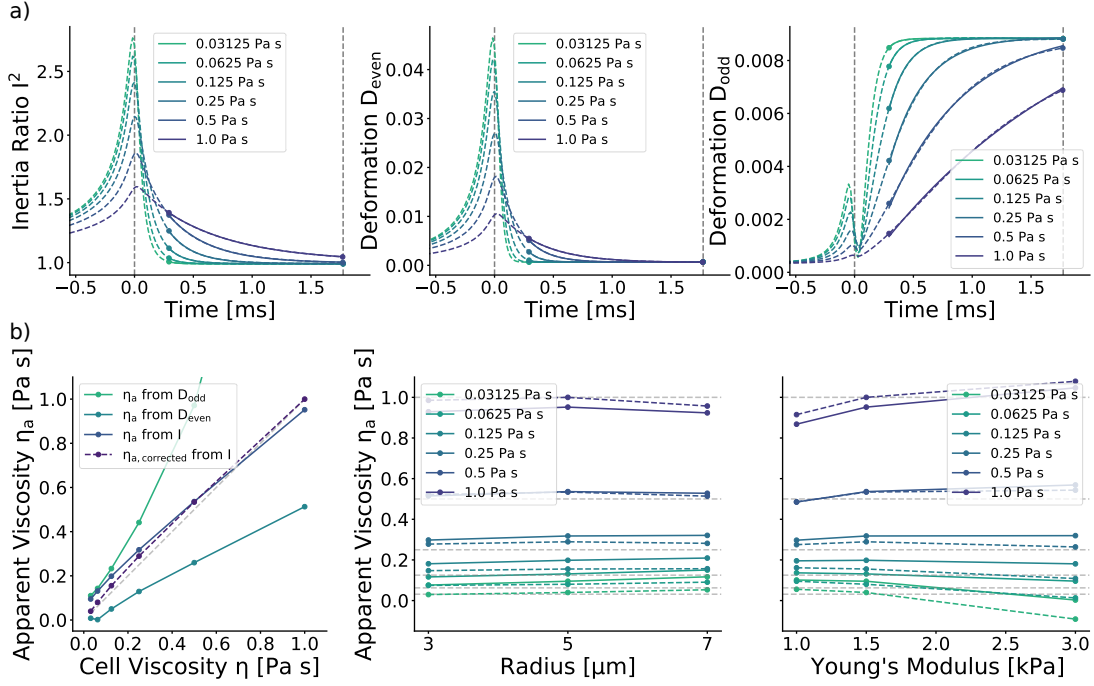


Figure 3.12: **Best Curve Fits and Apparent Viscosity:** **a) (left)** Squared inertia ratio I^2 (dashed lines) and the exponential fit (solid lines). The fitted interval is indicated by the circles starting at $50 \mu\text{m}$ until the end of the channel at $300 \mu\text{m}$. Here, only the inflow simulations are considered. Vertical grey dashed lines indicate the time of entrance and leaving of the narrow channel. **(middle)** Deformation D_{even} reconstructed from the even Fourier coefficients (dashed lines) and the exponential fit (solid lines). **(right)** Deformation D_{odd} reconstructed from the odd Fourier coefficients (dashed lines) and the exponential fit (solid lines). The cell radius and the Young's modulus is fixed to $r = 5 \mu\text{m}$ and $E = 1.5 \text{ Pa}$. **b) (left)** Apparent viscosity from the curve fits in a). The grey dashed line indicates agreement with the true viscosity of the cell. The radius is fixed to $r = 5 \mu\text{m}$ and the Young's modulus $E = 1.5 \text{ kPa}$ **(middle & right)** Apparent viscosity over the cell radius and Young's modulus based on the squared inertia ratio. The grey dashed lines indicate the true simulated viscosity. The dashed lines are the corrected apparent viscosity values based on the linear regression (see main text).

To improve the method of viscosity extraction even further, we applied linear regression with the radius r , the Young's modulus E and the apparent viscosity η_a as explanatory variables and the true viscosity η as the response. We obtain

$$\eta_{a,\text{corrected}} = -5.49 \times 10^{-3} * r - 1.82 \times 10^{-5} * E + 1.12 * \eta_a - 0.01,$$

where η_a is determined based on the inertia ratio, $\epsilon = I^2$ and the radius r is given in μm , the Young's modulus E in Pa, and the apparent viscosity η_a in Pa s. The corrected apparent viscosity is shown in Fig. 3.12b. The linear fit function gives an improved prediction of the actual viscosity with a coefficient of determination $R^2 = 0.98$. Still, there seems to be a non-linear influence pronounced especially for $E = 3 \text{ kPa}$ where the fit even yields negative viscosities.

We conclude that assuming a simple one-dimensional Kelvin-Voigt material model is too simplified for the complex three-dimensional interplay between the channel geometry, cell deformation and fluid flow. Yet, the approach presented here should be suitable to estimate cellular viscosity from the evolution of the inertia ratio after channel entry. This improves the results from Fregin et al. (2019) to a rigorous model-based approach for extraction of cellular viscosity from RT-DC measurements.

3.6. Approximation Error of the Cell Volume over the Channel

The volume of a cell in an RT-DC measurement is approximated by assuming a rotational symmetry of the cell along the x-axis. In our simulations, the cell shape and thus contours are convex and symmetrical to the x-axis. Under the assumption of axisymmetry an approximation to the cell volume can be obtained by rotating the two-dimensional cell contour which would be seen on a camera image. Considering only the upper (or lower) part of the contour given by the polygon of points (\bar{x}_i, \bar{y}_i) for $i = 0, \dots, \frac{N}{2} - 1$, centred around the barycentre of the contour (see above) the rotational approximation of the volume can be computed by e.g. the trapezoidal rule:

$$V_{\text{rot}} = \pi \int y^2 dx \approx \pi \sum_{i=1}^{\frac{N}{2}-1} \frac{\bar{y}_{i-1}^2 + \bar{y}_i^2}{2} \Delta \bar{x}_i,$$

where $\Delta \bar{x}_i = \bar{x}_i - \bar{x}_{i-1}$.

We define V_0 to be the (initial) volume of the cell, which is constant in time for an incompressible impermeable cell and plot the relative volume difference $\Delta V = \frac{V_{\text{rot}} - V_0}{V_0}$ over the channel in Fig. 3.13. The approximated volume V_{rot} is in good agreement for all three radii in the stationary state. For the cell with a Young's modulus of $E = 1$ kPa and a radius of $r = 7$ μm , the volume approximation of the stationary deformed cell is off by -1.6%. For all the other combinations shown here the approximation of the volume from the stationary deformed cell is below 0.5% (absolute value). At the inflow and outflow the rotational symmetry assumption does not hold, and we find large errors in the approximated volume. These errors increase with decreasing cell stiffness. For $E = 1$ kPa the cells are underestimated up to -27.2% at the inflow and overestimated up to 26.6% at the outflow. Accordingly, it is important to approximate the cells volume only in regions where the cell shapes can be assumed axisymmetric.

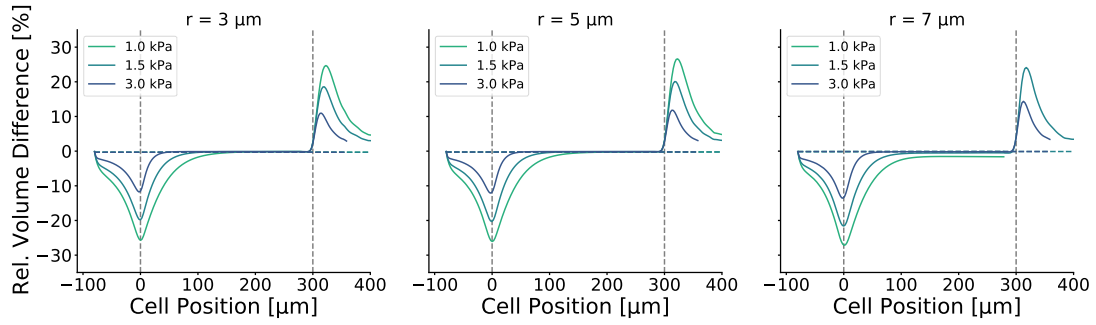


Figure 3.13: **Relative Volume Error over the Channel:** The relative error is derived by $\frac{V_{\text{rot}} - V_0}{V_0}$ where V_0 is the actual cell volume and V_{rot} its approximation by rotation of the cell contour projected in the x-y plane. The relative volume difference is in the range of $[-27.2, 26.2]\%$. The dotted lines are the relative volume changes of the incompressible cells in the numerical simulations.

To validate our numerical model we plot the actual relative volume change of the simulated incompressible cells in Fig. 3.13, too. The maximum error is below 0.32% for all configurations and is thus nicely conserved.

3.7. Conclusions

We performed the first three dimensional simulations of a cell traversing an RT-DC channel to obtain a better understanding of the complex interplay of transient hydrodynamics, cellular deformation and cell mechanical parameters. Based on the shear thinning rheology of the surrounding fluid, we looked at time-dependent behaviour of the cell which we assumed to be a viscoelastic Kelvin-Voigt bulk material. We find peak stresses at the inlet and outlet resulting in a peak cellular deformation whose size depends largely on the cell viscosity and elasticity. For high viscosities, the outlet peak is not present and the cells relax monotonically. As viscous cells with a viscosity of $\eta_c \geq 1 \text{ Pa s}$ do not reach stationary deformation within the narrow channel, the apparent Young's modulus can not be easily extracted in RT-DC measurements.

We compare with the 2D axisymmetric simulations similar to Schuster and Marti (2021) and found good agreement at the inlet with our full three dimensional model. The stationary deformation agrees for small and stiff (and thus less deforming) cells, too. Only for soft and bigger cells, the axisymmetric assumption does not hold any more and the square channel geometry needs to be taken into account. At the outlet, the influence of the square channel geometry does show a bigger influence on the deformation evolution and relaxation time.

Based on different deformation measures we extract the resulting apparent cell viscosity and find that the real viscosity is quite well recovered from the relaxation time of the inertia ratio. This significantly improves the results from Fregin et al. (2019) to a rigorous model-based approach for extraction of cellular viscosity from RT-DC measurements.

We conclude our virtual RT-DC analysis by looking at the approximated volume difference depending on the region in the RT-DC channel. This shows the limitation of axisymmetric approximations for those kind of simulations. With our simulation results, a more precise evaluation of RT-DC measurements is now possible, leading to more profound extraction of cell mechanical parameters from RT-DC measurements.

Appendix 3A. Derivation of the Deformation Measure from Cell Contours

All the deformation measures need to be derived from the images taken of the cells by the high-speed camera of the RT-DC setup. The resulting contours are given as a closed polygon with N points $(x_0, y_0), \dots, (x_{N-1}, y_{N-1})$ where $(x_0, y_0) = (x_{N-1}, y_{N-1})$.

For the deformation based on the circularity of the cell $D := 1 - \frac{2\sqrt{\pi A}}{L}$ (see (Otto et al., 2015)) we need the circumference L and the area A of the cell contour. Those quantities can be derived by

$$L = \sum_{i=0}^{N-1} \sqrt{(x_{i+1} - x_i)^2 + (y_{i+1} - y_i)^2}, \quad (3A.1)$$

$$A = \frac{1}{2} \sum_{i=0}^{N-1} (x_i y_{i+1} - x_{i+1} y_i). \quad (3A.2)$$

For the following deformation measure and the Fourier shape analysis, the cell contours need to be centred around their barycentre (x_b, y_b) . The barycentre can be calculated by $(x_b, y_b) = \left(\frac{I_x}{A}, \frac{I_y}{A}\right)$ where $I_x = \int_A x dA$ and $I_y = \int_A y dA$ are the integrals over the area enclosed by the polygon (Mokbel et al., 2017; Fregin et al., 2019):

$$I_x = \frac{1}{6} \sum_{i=0}^{N-1} (x_i y_{i+1} - x_{i+1} y_i) (x_i + x_{i+1}), \quad (3A.3)$$

$$I_y = \frac{1}{6} \sum_{i=0}^{N-1} (x_i y_{i+1} - x_{i+1} y_i) (y_i + y_{i+1}). \quad (3A.4)$$

We then define the centred cell contour as $(\bar{x}_i, \bar{y}_i) = (x_i - x_b, y_i - y_b)$ for $i = 0, \dots, N - 1$.

The inertia ratio – the ratio between the eigenvalues of the moment-of-area tensor – is defined by $I = \sqrt{\frac{I_{yy}}{I_{xx}}}$ with $I_{xx} = \int_A \bar{y}^2 dA$ and $I_{yy} = \int_A \bar{x}^2 dA$ if the cell contour is horizontally symmetric (Herbig et al., 2018). In this case, double integrals I_{xx} and I_{yy} can be derived by

$$I_{xx} = \frac{1}{12} \sum_{i=0}^{N-1} (\bar{x}_i \bar{y}_{i+1} - \bar{x}_{i+1} \bar{y}_i) (\bar{y}_i^2 + \bar{y}_i \bar{y}_{i+1} + \bar{y}_{i+1}^2), \quad (3A.5)$$

$$I_{yy} = \frac{1}{12} \sum_{i=0}^{N-1} (\bar{x}_i \bar{y}_{i+1} - \bar{x}_{i+1} \bar{y}_i) (\bar{x}_i^2 + \bar{x}_i \bar{x}_{i+1} + \bar{x}_{i+1}^2). \quad (3A.6)$$

Fourier Shape Descriptors

Similar to the inertia ratio, we derive the Fourier coefficients from the closed polygon (\bar{x}_i, \bar{y}_i) for $i = 0 \dots N$ centred around the cell barycentre (Fregin et al., 2019). First, we convert the contour into a sinusoidal signal by converting the contour points (\bar{x}_i, \bar{y}_i) into polar coordinates (r_i, φ_i) with $r_i = \sqrt{\bar{x}_i^2 + \bar{y}_i^2}$ and $\varphi_i = \arctan2(\bar{x}_i, \bar{y}_i)$ for $i = 0 \dots N$. The new function $r(\varphi)$ is sinusoidal and can be extended indefinitely. We linearly interpolate $r(\varphi)$ and resample the signal equidistantly over $\bar{\varphi} \in [-\pi, \pi]$ with $\Delta\bar{\varphi} = \frac{2\pi}{\bar{N}-1}$ where \bar{N} is the number of sample points to get $\bar{r}(\bar{\varphi})$.

The Fourier coefficients a_k and b_k can then be derived by

$$a_k = \frac{\Delta\bar{\varphi}}{\pi} \sum_{i=0}^{\bar{N}-1} \bar{r}_i \cos(k\bar{\varphi}_i) \quad k \geq 0, \quad (3A.7)$$

$$b_k = \frac{\Delta\bar{\varphi}}{\pi} \sum_{i=0}^{\bar{N}-1} \bar{r}_i \sin(k\bar{\varphi}_i) \quad k > 0. \quad (3A.8)$$

The coefficients a_k hold information about the size (a_0), the eccentricity (a_1), and ellipticity (a_2) of the cell contour, and higher order shape modes for $k > 3$ (Fregin et al., 2019). The coefficients b_k contain information about the angular orientation of the cell. Based on those coefficients, the contour $\tilde{r}(\tilde{\varphi})_{\text{even}}$ and $\tilde{r}(\tilde{\varphi})_{\text{odd}}$ can be obtained by applying the inverse discrete Fourier transform:

$$\tilde{r}(\tilde{\varphi})_{\text{even}} = \frac{a_0}{2} + \sum_{k=1}^k (a_{2k} \cos(2k\tilde{\varphi}_i) + a_{2k} \sin(2k\tilde{\varphi}_i)), \quad (3A.9)$$

$$\tilde{r}(\tilde{\varphi})_{\text{odd}} = \frac{a_0}{2} + \sum_{k=0}^k (a_{2k+1} \cos((2k+1)\tilde{\varphi}_i) + a_{2k+1} \sin((2k+1)\tilde{\varphi}_i)), \quad (3A.10)$$

where we set $\tilde{\varphi}_i = \varphi_i$. Here, we use only the first ten Fourier descriptors as in (Fregin et al., 2019) to reconstruct the contours.

ACKNOWLEDGEMENTS We thank the whole Guck-Lab at the MPL Erlangen for the discussion and valuable feedback. SA acknowledges support from the German Research Foundation DFG (grant AL1705/3) and support from the Saxon Ministry for Science and Art (SMWK MatEnUm-2 and EUProfil). Simulations were performed at the Center for Information Services and High Performance Computing (ZIH) at TU Dresden. LW thanks the COMSOL support staff for their excellent support.

References

- Binnig, G., Quate, C.F., Gerber, C., 1986. Atomic force microscope. *Phys. Rev. Lett.* 56, 930–933.
- Bonakdar, N., Gerum, R., Kuhn, M., Spörrer, M., Lippert, A., Schneider, W., Aifantis, K.E., Fabry, B., 2016. Mechanical plasticity of cells. *Nat. Mater.* 15, 1090–1094.
- Chan, C.J., Ekpenyong, A.E., Golfier, S., Li, W., Chalut, K.J., Otto, O., Elgeti, J., Guck, J., Lautenschläger, F., 2015. Myosin II Activity Softens Cells in Suspension. *Biophys. J.* 108, 1856–1869.
- Darling, E.M., Topel, M., Zauscher, S., Vail, T.P., Guilak, F., 2008. Viscoelastic properties of human mesenchymally-derived stem cells and primary osteoblasts, chondrocytes, and adipocytes. *J. Biomech.* 41, 454–464.
- Dupire, J., Puech, P.H., Helfer, E., Viallat, A., 2020. Mechanical adaptation of monocytes in model lung capillary networks. *Proc. Natl. Acad. Sci. U. S. A.* 117, 14798–14804.
- Ekpenyong, A.E., Whyte, G., Chalut, K., Pagliara, S., Lautenschläger, F., Fiddler, C., Paschke, S., Keyser, U.F., Chilver, E.R., Guck, J., 2012. Viscoelastic properties of differentiating blood cells are fate- and function-dependent. *PLoS One* 7, e45237.
- Fischer-Friedrich, E., Toyoda, Y., Cattin, C.J., Müller, D.J., Hyman, A.A., Jülicher, F., 2016. Rheology of the active cell cortex in mitosis. *Biophys. J.* 111, 589–600.
- Fletcher, D.A., Mullins, R.D., 2010. Cell mechanics and the cytoskeleton. *Nature* 463, 485–492.
- Fregin, B., Czerwinski, F., Biedenweg, D., Girardo, S., Gross, S., Aurich, K., Otto, O., 2019. High-throughput single-cell rheology in complex samples by dynamic real-time deformability cytometry. *Nat. Commun.* 10, 415.
- Guck, J., Ananthakrishnan, R., Mahmood, H., Moon, T.J., Cunningham, C.C., Käs, J., 2001. The optical stretcher: a novel laser tool to micromanipulate cells. *Biophys. J.* 81, 767–784.
- Guck, J., Ananthakrishnan, R., Moon, T.J., Cunningham, C.C., Käs, J., 2000. Optical deformability of soft biological dielectrics. *Phys. Rev. Lett.* 84, 5451–5454.
- Guck, J., Schinkinger, S., Lincoln, B., Wottawah, F., Ebert, S., Romeyke, M., Lenz, D., Erickson, H.M., Ananthakrishnan, R., Mitchell, D., Käs, J., Ulvick, S., Bilby, C., 2005. Optical deformability as an inherent cell marker for testing malignant transformation and metastatic competence. *Biophys. J.* 88, 3689–3698.
- Herbig, M., Mietke, A., Müller, P., Otto, O., 2018. Statistics for real-time deformability cytometry: Clustering, dimensionality reduction, and significance testing. *Biomicrofluidics* 12, 042214.
- Herold, C., 2017. Mapping of Deformation to Apparent Young’s Modulus in Real-Time Deformability Cytometry [arXiv:1704.00572](https://arxiv.org/abs/1704.00572).
- Hochmuth, R.M., 2000. Micropipette aspiration of living cells. *J. Biomech.* 33, 15–22.
- Kräter, M., Abuhattum, S., Soteriou, D., Jacobi, A., Krüger, T., Guck, J., Herbig, M., 2021. AIDeveloper: Deep learning image classification in life science and beyond. *Adv. Sci.*, 2003743.
- Lim, C.T., Zhou, E.H., Quek, S.T., 2006. Mechanical models for living cells—a review. *J. Biomech.* 39, 195–216.
- Mietke, A., Otto, O., Girardo, S., Rosendahl, P., Taubenberger, A., Golfier, S., Ulbricht, E., Aland, S., Guck, J., Fischer-Friedrich, E., 2015. Extracting cell stiffness from Real-Time deformability cytometry: Theory and experiment. *Biophys. J.* 109, 2023–2036.
- Mokbel, D., Abels, H., Aland, S., 2018. A phase-field model for fluid–structure interaction. *J. Comput. Phys.* 372, 823–840.
- Mokbel, M., Hosseini, K., Aland, S., Fischer-Friedrich, E., 2020. The poisson ratio of the cellular actin cortex is frequency dependent. *Biophys. J.* 118, 1968–1976.
- Mokbel, M., Mokbel, D., Mietke, A., Träber, N., Girardo, S., Otto, O., Guck, J., Aland, S., 2017. Numerical Simulation of Real-Time Deformability Cytometry To Extract Cell Mechanical Properties. *ACS Biomater Sci Eng* 3, 2962–2973.
- Müller, P., Herbig, M., O’Connell, E., Rosendahl, P., Schlögel, M., Guck, J., 2015. dclab version 0.34.1: Python library for the post-measurement analysis of real-time deformability cytometry data sets [software]. URL: <https://github.com/ZELLMECHANIK-DRESDEN/dclab>.
- Müller, S.J., Weigl, F., Bezold, C., Bächer, C., Albrecht, K., Gekle, S., 2021. A hyperelastic model for simulating cells in flow. *Biomech. Model. Mechanobiol.* 20, 509–520.
- Nawaz, A.A., Urbanska, M., Herbig, M., Nötzel, M., Kräter, M., Rosendahl, P., Herold, C., Toepfner, N., Kubánková, M., Goswami, R., Abuhattum, S., Reichel, F., Müller, P., Taubenberger, A., Girardo, S., Jacobi, A., Guck, J., 2020. Intelligent image-based deformation-assisted cell sorting with molecular specificity. *Nat. Methods* 17, 595–599.

- Nawaz, S., Sánchez, P., Bodensiek, K., Li, S., Simons, M., Schaap, I.A.T., 2012. Cell visco-elasticity measured with AFM and optical trapping at sub-micrometer deformations. *PLoS One* 7, e45297.
- Otto, O., Rosendahl, P., Mietke, A., Golfier, S., Herold, C., Klaue, D., Girardo, S., Pagliara, S., Ekpenyong, A., Jacobi, A., Wobus, M., Töpfner, N., Keyser, U.F., Mansfeld, J., Fischer-Friedrich, E., Guck, J., 2015. Real-time deformability cytometry: on-the-fly cell mechanical phenotyping. *Nat. Methods* 12, 199–202, 4 p following 202.
- Pegoraro, A.F., Janmey, P., Weitz, D.A., 2017. Mechanical properties of the cytoskeleton and cells. *Cold Spring Harb. Perspect. Biol.* 9.
- Radmacher, M., 2007. Studying the mechanics of cellular processes by atomic force microscopy. *Methods Cell Biol.* 83, 347–372.
- Rajagopal, V., Holmes, W.R., Lee, P.V.S., 2018. Computational modeling of single-cell mechanics and cytoskeletal mechanobiology. *Wiley Interdiscip. Rev. Syst. Biol. Med.* 10.
- Rheinlaender, J., Dimitracopoulos, A., Wallmeyer, B., Kronenberg, N.M., Chalut, K.J., Gather, M.C., Betz, T., Charas, G., Franze, K., 2020. Cortical cell stiffness is independent of substrate mechanics. *Nat. Mater.* 19, 1019–1025.
- Rosendahl, P., Plak, K., Jacobi, A., Kraeter, M., Toepfner, N., Otto, O., Herold, C., Winzi, M., Herbig, M., Ge, Y., Girardo, S., Wagner, K., Baum, B., Guck, J., 2018. Real-time fluorescence and deformability cytometry. *Nat. Methods* 15, 355–358.
- Schuster, R., Marti, O., 2021. Simulation of cell deformation inside a microfluidic channel to identify parameters for mechanical characterization of cells. *J. Phys. D Appl. Phys.* 54, 125401.
- Serrano-Alcalde, F., García-Aznar, J.M., Gómez-Benito, M.J., 2017. The role of nuclear mechanics in cell deformation under creeping flows. *J. Theor. Biol.* 432, 25–32.
- Taubenberger, A.V., Baum, B., Matthews, H.K., 2020. The mechanics of mitotic cell rounding. *Front Cell Dev Biol* 8, 687.
- Toepfner, N., Herold, C., Otto, O., Rosendahl, P., Jacobi, A., Kräter, M., Stächele, J., Menschner, L., Herbig, M., Ciuffreda, L., Ranford-Cartwright, L., Grzybek, M., Coskun, Ü., Reithuber, E., Garriss, G., Mellroth, P., Henriques-Normark, B., Tregay, N., Suttorp, M., Bornhäuser, M., Chilvers, E.R., Berner, R., Guck, J., 2018. Detection of human disease conditions by single-cell morpho-rheological phenotyping of blood. *Elife* 7, e29213.
- Urbanska, M., Muñoz, H.E., Shaw Bagnall, J., Otto, O., Manalis, S.R., Di Carlo, D., Guck, J., 2020. A comparison of microfluidic methods for high-throughput cell deformability measurements. *Nat. Methods* 17, 587–593.
- Urbanska, M., Winzi, M., Neumann, K., Abuhattum, S., Rosendahl, P., Müller, P., Taubenberger, A., Anastasiadis, K., Guck, J., 2017. Single-cell mechanical phenotype is an intrinsic marker of reprogramming and differentiation along the mouse neural lineage. *Development* 144, 4313–4321.
- Vicente-Manzanares, M., Sánchez-Madrid, F., 2004. Role of the cytoskeleton during leukocyte responses. *Nat. Rev. Immunol.* 4, 110–122.
- Wittwer, L.D., Müller, P., Mokbel, D., Mokbel, M., Guck, J., Aland, S., 2020. Finite element simulation data for the computation of the young's modulus in real-time deformability cytometry.
- Wu, P.H., Aroush, D.R.B., Asnacios, A., Chen, W.C., Dokukin, M.E., Doss, B.L., Durand-Smet, P., Ekpenyong, A., Guck, J., Guz, N.V., Janmey, P.A., Lee, J.S.H., Moore, N.M., Ott, A., Poh, Y.C., Ros, R., Sander, M., Sokolov, I., Staunton, J.R., Wang, N., Whyte, G., Wirtz, D., 2018. A comparison of methods to assess cell mechanical properties. *Nat. Methods* 15, 491–498.